Amyloid plaques drive long-range circuit reorganization in a mouse model of Alzheimer's disease

Zhao Z[1,2], Locascio J[1,2], Li H[1], Gowravaram N[1], Green RJ[1], Kastanenka KV[1,2], Bacskai B[1,2], Gomperts SN[1,2,*]

1. Department of Neurology, Mass General Brigham; Boston MA, 02114, USA
2. Harvard Medical School, Boston MA, 02115

* Corresponding author. Email: Gomperts.stephen@mgh.harvard.edu

ABSTRACT

Amyloid plaques are a pathological hallmark of Alzheimer's disease, but their specific contribution to widespread neuronal dysfunction remains unclear. Here, using a mouse model of Alzheimer's, we combine dynamic calcium imaging and electrophysiological recordings with co-registered plaque mapping to show how plaques affect hippocampal activity. We found that plaques provide nonlocal, long-range effects that depend on plaque characteristics and behavioral state. Place cells clustered near plaques, suggesting aberrant recruitment of plaque-adjacent neurons into spatial representations. In contrast, place cells before plaques formed had no spatial relationship to the location of future plaques. These results reveal a mechanism where local amyloid pathology reorganizes brain circuits, driving widespread dysfunction commensurate with cognitive impairment in Alzheimer's.

INTRODUCTION

Early in the course of Alzheimer's disease (AD), amyloid plaques composed of fibrillar species of amyloid-β42 (Aβ) deposit in the extracellular space, initiating a cascade that underlies hippocampal failure and memory loss. While much is known about the molecular mechanisms of AD pathology, the causes and circuit features of hippocampal disruption in AD are less well understood.

During exploratory behavior, many hippocampal neurons form spatial representations known as place fields, and these representations deteriorate in Aβ models of AD (*1*, *2*). Aberrantly hyperactive and silent subpopulations of neurons have also been observed in hippocampus and cortex of such AD models, implicating excitatory-inhibitory imbalance in Aβ-associated circuit failure (*3–5*). Fibrillar and oligomeric species of Aβ appear to contribute, as both have been shown to be neurotoxic and synaptotoxic (*6–15*).

In anesthetized AD model mice, aberrantly hyperactive cells have been found to cluster exclusively near amyloid plaques, while silent cells have been found to be widely distributed (*3*, *4*). However, as behavioral state critically influences hippocampal activity (*16–18*), and as anesthetics have complex effects on hemodynamics, neurophysiology, and calcium handling (*19–21*), it remains unknown whether this plaque-associated hyperactivity occurs during normal behaviors and across the sleep-wake cycle. Furthermore, the impact of such clustering of hyperactive cells near plaques on place coding has been unclear. Such hyperactivity could degrade place coding near plaques, but the opposite would be true if spatial tuning is preserved.

To investigate the spatial relationship of Aβ plaques and hippocampal neuronal activity across the sleep-wake cycle, we acquired dynamic calcium imaging and concomitant electrophysiological recordings in freely-behaving APP/PS1 mice, and then mapped neuronal activity and spatial representations to the local plaque topography. We found that plaques provide nonlocal, long-range effects that depend on plaque characteristics and behavioral state, thereby providing a critical window into the plaque-driven hippocampal circuit reorganization underlying cognitive impairment in Alzheimer's disease.

RESULTS

Spatial effects of amyloid plaques on neuronal activity depend on behavioral state

We acquired freely behaving hippocampal CA1 dynamic calcium imaging with GCaMP6f using the 1-photon (1P) Inscopix miniscope™ along with simultaneous, ipsilateral cortical and hippocampal local field potential (LFP) recordings of aged APP/PS1 mice (11 ± 0.3 months, n=7 mice), as animals explored a linear track (Run), subsequently rested in quiet wakefulness (QW), and transitioned into slow wave sleep (SWS) and rapid eye movement (REM) sleep (**Fig. 1A, B**). Dynamic calcium activity varied widely across cells and behavioral states, and we stratified cells by their activity within each state into the most active 5% ('hyperactive'), the least active ('hypoactive', < 1 event per 4 minutes (*16*, *18*)), and the remaining population of normally active cells. Examples of each cell type are shown in **Fig. 1B**, linked to the LFP recorded in each behavioral state. To map CA1 neuronal activity to plaque locations, mice then underwent 1P and 2P vascular imaging with Dextran Green, followed by 2P plaque imaging with methoxy-X04 (**Fig. 1A**). For spatial analyses, 1P neuronal and 2P plaque images were co-registered using the angiogram fiducials (**Fig. 1C; Suppl. Fig. 1**). In contrast to observations made in anesthetized AD mice that hyperactive cells are restricted to the immediate vicinity of amyloid plaques (*3*, *4*), hyperactive cells were detected at all distances from the nearest plaque in all behavioral states (**Fig. 1D**). This result persisted when hyperactivity was defined using an even more restrictive threshold: the top 1% of event rates for each state (**Suppl. Fig. 2**). On inspection, the proportion of hyperactive cells appeared to gradually diminish with distance from the nearest plaque in Run and SWS; while the proportion of hypoactive cells also appeared to gradually diminish with distance from the nearest plaque in Run. However, in a mixed effects model, using data from all animals across the distance bins and accounting for repeated measures by animal via a random intercept, hyperactive cells in Run alone showed a trend towards a negative relationship with distance from the nearest plaque ($\beta = -0.008$, $p = 0.08$; uncorrected for multiple comparisons across behavioral states and cell types).

Spatial profiles of CA1 dynamic calcium activity in amyloid plaque-laden AD mice varied across behavioral states (**Fig. 2A**). To evaluate how plaques impact local neuronal activity, we ran a backward eliminated mixed effects model for the dependent variable calcium event rate, using behavioral state (Run, QW, SWS, and REM) as a fixed predictor along with type of activity (hypoactive, normal, and hyperactive), the distance of each cell to the nearest plaque, and the distance of each cell to the nearest edge of the 2P field of view (edge distance) to account for the potential effects of plaques outside the field of view); as well as all 2-way interactions (see **Methods**). The model was significant, revealing several significant 2-way interactions, including of greatest interest, an interaction of distance to the nearest plaque and type of activity ($p<0.0001$) (**Fig. 2B, Suppl. Fig. 3A**). For hyperactive cells, proximity to plaques was associated with higher activity in all states, detectable over hundreds of microns. In

contrast, for hypoactive cells, proximity to plaques was associated with lower activity in Run, with minimal effect in other behavioral states. For normally active cells, proximity to amyloid plaques was associated with slightly lower neuronal activity in Run, and slightly higher activity in states of QW, SWS, and REM sleep.

The model also identified a 2-way interaction of behavioral state and activity type ($p<0.0001$), such that cells most (or least) active in a given state did not maintain their activity type across behavioral states. In addition, there was an interaction of distance to the nearest plaque and behavioral state ($p<0.0001$) (**Fig. 2B**). Finally, the model detected a shallow but significant interaction of edge distance and activity type ($p=0.0065$), consistent with the contribution of plaques outside the field of view, such that with greater distance from the edge, the activity of hyperactive cells slightly diminished, the activity of hypoactive cells slightly increased, while the activity of normally active cells remained largely unchanged (**Suppl. Fig. 3B**). The proportion of the variance accounted for by fixed effects in this model was 51.7%.

Spatial effects of amyloid plaques depend on their size and axial position in CA1

Amyloid plaques varied by size and axial position within CA1, with some centered in the pyramidal cell layer while others were located in the dendritic layers of s. radiatum and s. oriens (**Fig. 3A**). As amyloid plaques have been shown to disrupt both the neuronal processes that traverse them (*22*) and local inhibitory synapses (*23*), we set out to determine if plaque size or axial position within CA1 affected neuronal activity. To do so, we dichotomized plaques by size as well as by their axial position (pyramidal cell layer vs. dendritic layers; **Fig. 3B**), and we extended the above mixed effects model to include size and axial position of the nearest plaque (see **Methods**). In addition to the same significant 2-way interactions described above, the model detected a significant 3-way interaction of plaque axial position, plaque size, and distance to the nearest plaque ($p=0.0039$). Specifically, large amyloid plaques (define size here) of the pyramidal cell layer were associated with the highest activity of plaque-adjacent neurons and the steepest decline in activity with distance (**Fig. 3C**). Small plaques of the pyramidal cell layer were intermediate, while dendritic plaques were associated with the smallest effect of plaque adjacent neurons on activity (**Fig. 3C**). There was also a small but significant interaction of plaque axial position and edge distance ($p<0.0001$), as well as a modest interaction of activity type and edge distance ($p<0.0046$) similar to that observed in the previous model (**Suppl. Fig. 4**). The model accounted for 51.8% of the variance.

Amyloid plaque-driven changes in local spatial encoding

As spatial memory impairment is a hallmark of AD (*24*) and hippocampal place cell recruitment during navigation plays an important role in spatial memory formation (*25*), we next evaluated the local impact of amyloid plaques on hippocampal spatial representations. APP/PS1 mice had a decreased proportion of place cells compared to nontransgenic wildtype mice (APP/PS1 vs WT: 11.7 ± 2.3% vs 24.5 ± 2.7%, Mann-Whitney U test, $p = 0.03$; **Fig. 4A, B, C**). To evaluate whether amyloid plaques influenced the spatial distribution of place cells, we first compared the distance between place cells in APP/PS1 and WT mice. Compared to WT mice, the distribution of place cell distances in APP/PS1 mice over-represented short distances, consistent with clusters evident on inspection (Kolmogorov-Smirnov test, p = 4.09 x 10-15; **Fig. 4D, E**).

To determine whether amyloid plaques contributed to this clustering, we ran a backward elimination mixed effects model to determine whether proximity to amyloid plaques influenced place cell identity. The fixed effect predictors were distance to the nearest plaque, the nearest plaque axial position (cell layer vs. dendritic layers), nearest plaque size (big vs. small), distance to the edge of the field of view (edge distance), and all two-way interactions. The dependent variable was the binary variable of place cell identity (Yes/No). This analysis revealed a significant interaction between distance to the nearest plaque and edge distance ($p<0.0001$), reflecting an increasing probability of place cell identity with decreasing distance to the nearest plaque, with the rate of this increase growing more pronounced towards the center of the field of view (**Fig. 4F**). There was also a main effect for plaque axial position, with the probability of place cell identity higher near plaques of the dendritic layers than the pyramidal cell layer ($p=0.005$).

In contrast to place cell identity, we found no significant effect of proximity to amyloid plaques on place cell spatial information when we ran an analogous model (**Methods**; **Suppl. Fig. 5**). Together, these results show that place cells cluster near amyloid plaques.

Place cell locations do not detectably impact future amyloid plaque locations

Neuronal activity drives release of Aβ42 (*26*) and contributes to Aβ42 concentration in interstitial fluid (*27*). To differentiate between the possibility that place cells tend to aggregate near amyloid plaques, and the complementary possibility that place cell clusters arise in AD mice before plaques form and drive their future deposition, we acquired dynamic calcium imaging in CA1 of young AD mice (age 5.4 ± 0.16

months, n=3) prior to plaque formation, and related the location of place cells to the location of future plaques, imaged in the same animals at age 10.5 ± 0.19 months. Angiogram fiducials at the two timepoints were used to co-register the young 1P dynamic calcium imaging of neuronal activity and the old 2P imaging of amyloid plaques (**Methods**; **Fig. 5A; Suppl. Fig. 6)**. We ran a mixed effects analysis for the dependent variable distance to the nearest future plaque, with the binary fixed predictor of pre-plaque place cell identity (Yes/No) (see **Methods**). This analysis showed that place cell identity before plaques formed was not a significant predictor of future plaque location (**Fig. 5B**). When we ran a complementary set of analyses relating dynamic calcium rates in each behavioral state before plaques form to future plaque locations, higher activity in SWS but not in Run, QW, or REM sleep was weakly predictive of future plaque locations (p=0.038; **Fig. 5C**).

DISCUSSION

While AD is associated with progressive hippocampal failure, how amyloid plaques influence spatial coding in their local microenvironment has been unclear. Here, we show that amyloid plaques exert long-range effects both on aberrant neuronal activity across behavioral states as well as on place cell coding. With the progressive accumulation of amyloid plaques in AD, these disruptive effects on hippocampal function are likely to contribute to increasing hippocampal failure.

Place coding is a key function of the hippocampus, and its deterioration in AD patients and in AD models is well established (*24*). The biased recruitment of plaque-adjacent cells into the representation of space is well-positioned to underlie this degraded place coding. With accumulation of amyloid plaques in AD, excessive reliance on a reduced pool of available neurons to represent space within and across environments would be expected to progressively impair both hippocampal remapping and pattern separation, fundamental features of hippocampal mnemonic function (*28*).

Our results also suggest that amyloid plaques drive the clustering of place cells rather than vice versa, as our longitudinal studies did not detect a predictive effect of place cell locations on future plaque positions. Although the mechanisms underlying the clustering of place cells near amyloid plaques are unknown, loss of inhibitory synapses in the region around amyloid plaques, as recently reported (*23*), is likely to contribute, as may the disruption of morphology of local processes (*22*).

Unexpectedly, we detected long range gradients of neuronal activity centered on amyloid plaques rather than highly local plaque effects. Although the biological basis of these effects is not yet clear, we

anticipate that spatial gradients of plaque-derived soluble Aβ oligomers may contribute, as Aβ oligomers have been shown to be toxic, impair synaptic activity and degrade hippocampal function, potentially even before plaques predominate (*6–15*).

Prior reports of aberrantly high and low activity of hippocampal and cortical neurons in amyloid plaque-bearing AD models have supported the concept of perturbed excitatory-inhibitory balance in AD (*3–5*). We and others have found that behavioral state has a marked effect on such imbalance (*17*). The present results extend these findings, showing that the spatial effects of plaques on neuronal activity are also markedly state-dependent. In Run behavior, aberrant hyper- and hypoactivity was greatest close to plaques. However, plaque-associated hyperactivity declined faster with distance from plaques in non-Run states than in Run, and hypoactivity was unaffected by plaque proximity in non-Run states.

Consistent with the toxicity of Aβ and the local impact of amyloid plaques on the brain parenchyma, large plaques were more disruptive than small plaques on neuronal activity. Interestingly, large plaques deposited in the pyramidal cell layer were most disruptive, while plaques in the dendritic layers were least disruptive. In contrast, we observed that place cells clustered more around dendritic layer plaques than cell layer plaques. These observations may reflect differential effects on inhibitory versus excitatory synapses, given their axial distribution within CA1 (*29*) as well as the possible contribution of local inhibitory synapse losses, which are particularly enriched around pyramidal cell somas (*23, 30*).

Intriguingly, we found that the locations of hyperactive cells in SWS predicted future plaque locations, albeit weakly. As SWS is the one behavioral state associated with amyloid clearance (*31*, *32*), it is possible that release of Aβ in SWS by such hyperactive cells overwhelms local clearance mechanisms, enabling local Aβ concentrations to rise above the local critical threshold for oligomerization and deposition. Future work is needed to evaluate this idea.

Key strengths of this study include linking spatial representations and neuronal activity across behavioral states to the local influence of amyloid plaques in the hippocampus, a region involved in early AD pathology and memory loss. A further strength was the use of 2p microscopy to images amyloid plaques, providing an accurate assessment of plaque burden across the axial extent of CA1. Limitations of this study include the use of dynamic calcium imaging to identify place cells, rather than single unit electrophysiology. Even so, dynamic calcium imaging has proven to be a robust measure of

neuronal activity and place cell physiology, enabling the simultaneous study of large numbers of CA1 neurons (*16–18*). Co-registration of 1P and 2P datasets using angiogram fiducials was associated with low error. Although sample sizes of mice were modest, we were able to sample 85 plaques and 3762 neurons across behavioral states. Another limitation was the inability to assess the effects of amyloid plaques on calcium in non-somatic cellular compartments (*28*). In addition, AD is characterized by both the deposition of amyloid plaques and the intracellular accumulation of neurofibrillary tangles, and future work evaluating the added contribution of tau will be informative.

Together, the present findings show that amyloid plaques are associated with state-dependent, long-range spatial gradients of neuronal activity, and with local clustering of place cells. These effects are anticipated to contribute to the progressive impairment of hippocampal-dependent memory in AD.

METHODS

All procedures were approved by the Institutional Animal Care and Use Committees of the Massachusetts General Hospital. The study was conducted in accordance with the ethical guidelines of the US National Institutes of Health.

Surgical preparation

The APP/PS1 mouse strain used for this research project, B6C3-Tg(APPswe,PSEN1dE9)85Dbo/Mmjax, RRID:MMRRC_034829-JAX, was purchased from the Mutant Mouse Resource and Research Center (MMRRC) at The Jackson Laboratory, an NIH-funded strain repository, and was donated to the MMRRC by David Borchelt, Ph.D., McKnight Brain Institute, University of Florida (*33*). Surgical preparation has been previously prescribed (*16*, *18*). Briefly, APP/PS1 mice and their age/sex matched non-transgenic control littermates underwent injection of 1 μL AAV-hSyn-GCaMP6f (Addgene, titer > $7x10^{12}$ vg/ml) into the hippocampal CA1 region (AP -2.1 mm, ML -1.65 mm, DV 1.4 mm from bregma) under anesthesia (isoflurane 1.5-2%). A gradient index (GRIN) lens (1 mm diameter, AP -2.1 mm, ML -1.50 mm, DV -1.2 mm from bregma) and a custom drivable probe holding 7 stereotrodes (AP -2.8 mm, ML 2.6 mm, -36° relative to the AP axis, -39° relative to the inter-aural axis; DV 1.2 mm) were implanted ipsilaterally 2 weeks later with cerebellar ground. The microscope baseplate was attached three weeks later. Animals were housed in individual cages with a 12 hr light/12hr dark standard light cycle.

1P Dynamic calcium imaging and electrophysiology recordings

The Inscopix™ nVista3 mini-microscope and acquisition system (IDAS) were used for dynamic calcium imaging, sampling at 20 fps. Local field potential (LFP) (Neuralynx™) was sampled at 32 kHz followed by 0.5-900 Hz filtering and down sampling to 1000 Hz. Animal position was measured with overhead camera tracking of two LED diodes mounted on the headstage. Electrophysiological recordings and position sampling were acquired continuously. Simultaneous dynamic calcium imaging was acquired in 10-min ON and 5-min OFF blocks to avoid photobleaching and was synchronized with electrophysiological data with TTL pulses (*16*, *18*).

Behavior and sleep staging

Data were acquired as animals explored a linear track and were then moved to their home cage within the same recording room to sample subsequent quiet wakefulness (QW), slow-wave sleep (SWS), and REM sleep. Cortical delta (1-4 Hz), hippocampal theta (4-10 Hz) and ripples (100-300 Hz), and rat position and posture were used to identify behavioral states: Run was defined as animals explored the linear track with speeds exceeding 1 cm/sec and was characterized by a strong theta oscillation; QW was identified when animals were stationary (< 0.5 cm/sec) for at least 5 seconds with their eyes open; SWS was identified by the presence of sharp wave ripples (SWRs) and high delta/theta LFP power ratio (>2) in animals in a sleep posture; REM sleep was identified as epochs of high theta/delta LFP power ratio (>2) in animals in a sleep posture (*18*).

2P imaging of amyloid plaques and acquisition of angiograms

Following 1P imaging of dynamic calcium activity, Methoxy-X04 (10 mg/kg, i.p.) was injected to label amyloid plaques (*34*). For 1P vascular imaging at least one day later, animals were then lightly anesthetized with isoflurane (~1.5%; with concentration sufficient to inhibit dynamic calcium activity) and fluorescein dextran (0.3 ml, i.v.) was injected into the tail vein and imaging was acquired. Animals were then transferred to a 2P microscope and head-fixed for 2P vascular and amyloid plaque imaging on a commercial multiphoton system as previously described (*35*) (Olympus Fluoview 1000MPE) mounted on an Olympus BX61WI upright microscope. A mode-locked titanium/sapphire laser (MaiTai; Spectra-Physics, Fremont, CA) was used to generate two-photon fluorescence with 800 nm excitation. Detectors consisting of photomutliplier tubes (Hamamatsu, Ichinocho, Japan) collected light in the following ranges: 380-480 and 500-540 nm. 2P imaging with 800 nm excitation of hippocampal CA1 was acquired through the GRIN lens, acquiring a stack of images spanning the CA1 cell layer, across 150 μm.

Data analysis. All analyses were performed using MATLAB, Python, or SAS unless specified otherwise (*16–18*).

Calcium imaging: Inscopix Data Processing Software (IDPS, Inscopix, Palo Alto, California) was used for movie preprocessing, spatial filtering, motion correction, normalization ΔF/F, and constrained non-negative matrix factorization (CNMFE) cell identification (*36*). Each identified cell was manually examined and accepted with oval cell shape and high signal-noise-ratio (SNR). Calcium events were then detected at 2 Z scores above the mean, with onset defined at 30% of peak amplitude (*16–18*). Low rate cells were defined as < 0.25 transients/min (*16–18*); high rate cells were defined using a calcium event rate threshold set at the top 5% of calcium rates for each behavioral state of each animal.

Place cell: Spatial tuning curves (3 cm bins) were constructed for each cell for each running direction (LR and RL) using all detected calcium events acquired during running (velocity > 1 cm/s). Spatial information was measured for each cell as the amount of information (in bits) conveyed per calcium event, and was compared to 1000 shuffled spatial information distributions to test significance (Monte Carlo p-value < 0.05) (*37*), and taken as the larger of the LR and the RL trajectories.

Single timepoint 2P-1P image co-registration: Custom Python code was used to co-register 1P and 2P angiograms, implementing a coherent point drift algorithm and Python package pycpd 2.0.0 (*38, 39*). In brief, landmark points marked on 1P and 2P angiograms were used to compute the parameters for a similarity transformation (that included translation, rotation, and scaling) that maximized their overlap. These transformation parameters were then applied to the 1P angiograms and dynamic calcium imaging data to register them in the 2P space. Co-registration accuracy was quantified by calculating the nearest-neighbor distance between corresponding features of the transformed 1P and 2P angiogram datasets. Across the datasets, the root mean square error (RMSE) was 1.9 ± 0.08 µm.

Young 1P- old 2P image co-registration: The spatial alignment of 1P young calcium imaging data and 2P amyloid plaque image stacks was achieved through a two-stage registration procedure. Stage 1: Longitudinal 1P image co-registration. First, a similarity transformation was computed to align the initial angiogram (1P young) with the follow-up angiogram (1P old). Landmark Selection: Corresponding anatomical landmarks were identified on both the 1P young and 1P old angiograms. These landmarks were used to compute the parameters for a first similarity transformation, which included translation, rotation, and uniform scaling. The transformation parameters were optimized to maximize the spatial overlap of the landmark points. The calculated transformation was then applied to the 1P young angiogram and its associated dynamic calcium imaging data, registering them into the coordinate space of the 1P old angiogram. Stage 2: 2P-1P image co-registration. To integrate the 1P and 2P datasets, a second registration was performed. A new set of landmarks was selected from major vessels that

maintained a consistent structural configuration across the registered 1P young and 2P old angiograms. A second similarity transformation was computed using these stable landmarks to maximize the overlap between the registered 1P young angiogram and the 2P old angiogram. This second set of transformation parameters was then applied to the registered 1P young angiogram and dynamic calcium imaging data to map them into the 2P coordinate space. To evaluate the accuracy of this co-registration method, we computed the nearest-neighbor distance between corresponding features of the transformed 1P young and transformed 1P old angiograms (**Suppl. Fig. 6A**). Across all datasets, the RMSE of this distance was 13.4 ± 0.19 µm (**Suppl. Fig. 6D**). The region of vessels used for this transformation accounted for 71.4 ± 3.1% of the area of imaged neurons and amyloid plaques (**Suppl. Fig. 6B,C**).

Statistical analyses.

Dynamic calcium activity as a function of proximity to amyloid plaques was assessed using a backward eliminated Mixed Effects Model for the dependent variable "Calcium Rate", using the "State" (Run, QW, SWS, and REM) as a fixed predictor along with Type of Activity (Hypo, Normal, and Hyper), the Distance to the nearest plaque, and Edge Distance, including all 2-way interactions. The random effect was Mouse. Effect of plaque size and hippocampal axial position on dynamic calcium activity was assessed by adding plaque size (big vs. small) and hippocampal axial position (pyramidal cell layer vs. dendritic layers), their interaction, and the interactions of these two terms with Distance to the nearest plaque and Edge Distance to the above model. Place cell identity and place cell spatial information as a function of proximity to amyloid plaques were assessed with two backward elimination mixed effects models: For both, the fixed effect predictors were: Distance to the nearest plaque, the nearest plaque axial position, nearest plaque size, and distance to the edge of the field of view (edge distance), and all two-way interactions. The Random Term was Mouse. The dependent variable for the first analysis was the binary variable of Place Cell Identity (Yes/No=1/0), and the dependent variable for the second analysis was Spatial Information. Because the dependent variable was binary in the former case, a Generalized Linear Mixed Model was run assuming a binomial distribution and a logit link function for the dependent variable. Place cell identity as a function of proximity to future amyloid plaques was assessed with a mixed effects GLM for the binary dependent variable of pre-plaque Place Cell Identity (Yes/No; measured at timepoint 1). The fixed effect predictor was Distance to Nearest Future Plaque at timepoint 2. The Random Term was Mouse. The GLM assumed a binary distribution and a logit link function for the dependent variable. Effect of dynamic calcium activity on proximity to future amyloid plaques was assessed with a mixed effects model for the dependent variable of Distance to Nearest Plaque at timepoint

2, using the Run, QW, SWS, and REM Calcium Rate (in separate analyses) as a fixed predictor with Distance to Nearest Future Plaque at timepoint 2. The Random Term was Mouse.

REFERENCES

1. H. Jun, A. Bramian, S. Soma, T. Saito, T. C. Saido, K. M. Igarashi, Disrupted Place Cell Remapping and Impaired Grid Cells in a Knockin Model of Alzheimer's Disease. *Neuron* **107**, 1095-1112.e6 (2020).

2. A. J. Mably, B. J. Gereke, D. T. Jones, L. L. Colgin, Impairments in spatial representations and rhythmic coordination of place cells in the 3xTg mouse model of Alzheimer's disease. *Hippocampus* **27**, 378–392 (2017).

3. M. A. Busche, G. Eichhoff, H. Adelsberger, D. Abramowski, K.-H. Wiederhold, C. Haass, M. Staufenbiel, A. Konnerth, O. Garaschuk, Clusters of Hyperactive Neurons Near Amyloid Plaques in a Mouse Model of Alzheimer's Disease. *Science* **321**, 1686–1689 (2008).

4. M. A. Busche, X. Chen, H. A. Henning, J. Reichwald, M. Staufenbiel, B. Sakmann, A. Konnerth, Critical role of soluble amyloid-β for early hippocampal hyperactivity in a mouse model of Alzheimer's disease. *Proc. Natl. Acad. Sci. U.S.A.* **109**, 8740–8745 (2012).

5. M. A. Busche, A. Konnerth, Neuronal hyperactivity--A key defect in Alzheimer's disease? *Bioessays* **37**, 624–632 (2015).

6. M. Arbel-Ornath, E. Hudry, J. R. Boivin, T. Hashimoto, S. Takeda, K. V. Kuchibhotla, S. Hou, C. R. Lattarulo, A. M. Belcher, N. Shakerdge, P. B. Trujillo, A. Muzikansky, R. A. Betensky, B. T. Hyman, B. J. Bacskai, Soluble oligomeric amyloid-β induces calcium dyshomeostasis that precedes synapse loss in the living mouse brain. *Mol Neurodegener* **12**, 27 (2017).

7. J. P. Cleary, D. M. Walsh, J. J. Hofmeister, G. M. Shankar, M. A. Kuskowski, D. J. Selkoe, K. H. Ashe, Natural oligomers of the amyloid-beta protein specifically disrupt cognitive function. *Nat Neurosci* **8**, 79–84 (2005).

8. E. N. Cline, M. A. Bicca, K. L. Viola, W. L. Klein, The Amyloid-β Oligomer Hypothesis: Beginning of the Third Decade. *J Alzheimers Dis* **64**, S567–S610 (2018).

9. Y. Ding, J. Zhao, X. Zhang, S. Wang, K. L. Viola, F. E. Chow, Y. Zhang, C. Lippa, W. L. Klein, Y. Gong, Amyloid Beta Oligomers Target to Extracellular and Intracellular Neuronal Synaptic Proteins in Alzheimer's Disease. *Front Neurol* **10**, 1140 (2019).

10. P. Faucher, N. Mons, J. Micheau, C. Louis, D. J. Beracochea, Hippocampal Injections of Oligomeric Amyloid β-peptide (1-42) Induce Selective Working Memory Deficits and Long-lasting Alterations of ERK Signaling Pathway. *Front Aging Neurosci* **7**, 245 (2015).

11. S. T. Ferreira, M. V. Lourenco, M. M. Oliveira, F. G. De Felice, Soluble amyloid-β oligomers as synaptotoxins leading to cognitive impairment in Alzheimer's disease. *Front Cell Neurosci* **9**, 191 (2015).

12. O. Nicole, S. Hadzibegovic, J. Gajda, B. Bontempi, T. Bem, P. Meyrand, Soluble amyloid beta oligomers block the learning-induced increase in hippocampal sharp wave-ripple rate and impair spatial memory formation. *Sci Rep* **6**, 22728 (2016).

13. G. G. Özcan, S. Lim, P. L. Leighton, W. T. Allison, J. Rihel, Sleep is bi-directionally modified by amyloid beta oligomers. *Elife* **9**, e53995 (2020).

14. G. M. Shankar, S. Li, T. H. Mehta, A. Garcia-Munoz, N. E. Shepardson, I. Smith, F. M. Brett, M. A. Farrell, M. J. Rowan, C. A. Lemere, C. M. Regan, D. M. Walsh, B. L. Sabatini, D. J. Selkoe, Amyloid-beta protein dimers isolated directly from Alzheimer's brains impair synaptic plasticity and memory. *Nat Med* **14**, 837–842 (2008).

15. R. Malinow, R. C. Malenka, AMPA receptor trafficking and synaptic plasticity. *Annu Rev Neurosci* **25**, 103–126 (2002).

16. H. Zhou, K. R. Neville, N. Goldstein, S. Kabu, N. Kausar, R. Ye, T. T. Nguyen, N. Gelwan, B. T. Hyman, S. N. Gomperts, Cholinergic modulation of hippocampal calcium activity across the sleep-wake cycle. *Elife* **8**, e39777 (2019).

17. H. Zhou, H. Li, N. Gowravaram, M. Quan, N. Kausar, S. N. Gomperts, Disruption of hippocampal neuronal circuit function depends upon behavioral state in the APP/PS1 mouse model of Alzheimer's disease. *Sci Rep* **12**, 21022 (2022).

18. H. Li, Z. Zhao, A. Fassini, H. K. Lee, R. J. Green, S. N. Gomperts, Impaired hippocampal circuit function underlying memory encoding and consolidation precede robust Aβ deposition in a mouse model of alzheimer's disease. *Sci Rep* **15**, 21957 (2025).

19. K. Krnjević, Cellular and synaptic actions of general anaesthetics. *Gen Pharmacol* **23**, 965–975 (1992).

20. L. P. Munting, M. P. P. Derieppe, E. Suidgeest, B. Denis de Senneville, J. A. Wells, L. van der Weerd, Influence of different isoflurane anesthesia protocols on murine cerebral hemodynamics measured with pseudo-continuous arterial spin labeling. *NMR Biomed* **32**, e4105 (2019).

21. B. Lustig, Y. Wang, E. Pastalkova, Oscillatory patterns in hippocampus under light and deep isoflurane anesthesia closely mirror prominent brain states in awake animals. *Hippocampus* **26**, 102–109 (2016).

22. R. B. Knowles, C. Wyart, S. V. Buldyrev, L. Cruz, B. Urbanc, M. E. Hasselmo, H. E. Stanley, B. T. Hyman, Plaque-induced neurite abnormalities: implications for disruption of neural networks in Alzheimer's disease. *Proc Natl Acad Sci U S A* **96**, 5274–5279 (1999).

23. H. Kurucu, M. Colom-Cadena, C. Davies, L. Wilkins, D. King, J. Rose, M. Tzioras, J. H. Tulloch, C. Smith, T. L. Spires-Jones, Inhibitory synapse loss and accumulation of amyloid beta in inhibitory presynaptic terminals in Alzheimer's disease. *Eur J Neurol* **29**, 1311–1323 (2022).

24. A. Silva, M. C. Martínez, Spatial memory deficits in Alzheimer's disease and their connection to cognitive maps' formation by place cells and grid cells. *Front Behav Neurosci* **16**, 1082158 (2022).

25. G. Girardeau, V. Lopes-Dos-Santos, Brain neural patterns and the memory function of sleep. *Science* **374**, 560–564 (2021).

26. J. R. Cirrito, K. A. Yamada, M. B. Finn, R. S. Sloviter, K. R. Bales, P. C. May, D. D. Schoepp, S. M. Paul, S. Mennerick, D. M. Holtzman, Synaptic activity regulates interstitial fluid amyloid-beta levels in vivo. *Neuron* **48**, 913–922 (2005).

27. A. W. Bero, P. Yan, J. H. Roh, J. R. Cirrito, F. R. Stewart, M. E. Raichle, J.-M. Lee, D. M. Holtzman, Neuronal activity regulates the regional vulnerability to amyloid-β deposition. *Nat Neurosci* **14**, 750–756 (2011).

28. *The Hippocampus Book* (Oxford University Press, Oxford, 2007).

29. M. Megías, Z. Emri, T. F. Freund, A. I. Gulyás, Total number and distribution of inhibitory and excitatory synapses on hippocampal CA1 pyramidal cells. *Neuroscience* **102**, 527–540 (2001).

30. M. Montero-Crespo, M. Domínguez-Álvaro, L. Alonso-Nanclares, J. DeFelipe, L. Blazquez-Llorca, Three-dimensional analysis of synaptic organization in the hippocampal CA1 field in Alzheimer's disease. *Brain* **144**, 553–573 (2021).

31. L. Xie, H. Kang, Q. Xu, M. J. Chen, Y. Liao, M. Thiyagarajan, J. O'Donnell, D. J. Christensen, C. Nicholson, J. J. Iliff, T. Takano, R. Deane, M. Nedergaard, Sleep drives metabolite clearance from the adult brain. *Science* **342**, 373–377 (2013).

32. J. H. Roh, Y. Huang, A. W. Bero, T. Kasten, F. R. Stewart, R. J. Bateman, D. M. Holtzman, Disruption of the sleep-wake cycle and diurnal fluctuation of β-amyloid in mice with Alzheimer's disease pathology. *Sci Transl Med* **4**, 150ra122 (2012).

33. J. L. Jankowsky, H. H. Slunt, T. Ratovitski, N. A. Jenkins, N. G. Copeland, D. R. Borchelt, Co-expression of multiple transgenes in mouse CNS: a comparison of strategies. *Biomol Eng* **17**, 157–165 (2001).

34. W. E. Klunk, B. J. Bacskai, C. A. Mathis, S. T. Kajdasz, M. E. McLellan, M. P. Frosch, M. L. Debnath, D. P. Holt, Y. Wang, B. T. Hyman, Imaging Abeta plaques in living transgenic mice with multiphoton microscopy and methoxy-X04, a systemically administered Congo red derivative. *J Neuropathol Exp Neurol* **61**, 797–805 (2002).

35. Y. F. Lee, A. N. Russ, Q. Zhao, S. J. Perle, M. Maci, M. R. Miller, S. S. Hou, M. Algamal, Z. Zhao, H. Li, N. Gelwan, Z. Liu, S. N. Gomperts, A. Araque, E. Galea, B. J. Bacskai, K. V. Kastanenka, Optogenetic targeting of astrocytes restores slow brain rhythm function and slows Alzheimer's disease pathology. *Sci Rep* **13**, 13075 (2023).

36. P. Zhou, S. L. Resendez, J. Rodriguez-Romaguera, J. C. Jimenez, S. Q. Neufeld, A. Giovannucci, J. Friedrich, E. A. Pnevmatikakis, G. D. Stuber, R. Hen, M. A. Kheirbek, B. L. Sabatini, R. E. Kass, L. Paninski, Efficient and accurate extraction of in vivo calcium signals from microendoscopic video data. *Elife* **7**, e28728 (2018).

37. E. J. Markus, C. A. Barnes, B. L. McNaughton, V. L. Gladden, W. E. Skaggs, Spatial information content and reliability of hippocampal CA1 neurons: effects of visual input. *Hippocampus* **4**, 410–421 (1994).

38. A. Myronenko, X. Song, Point-Set Registration: Coherent Point Drift. *IEEE Trans. Pattern Anal. Mach. Intell.* **32**, 2262–2275 (2010).

39. A. A. Gatti, S. Khallaghi, PyCPD: Pure NumPy Implementation of the Coherent PointDrift Algorithm. *JOSS* **7**, 4681 (2022).

Acknowledgements

We thank Brad Hyman for review of the manuscript.

Funding: R01 AG054551; R01 AG077611

Author contributions

Conceptualization, Z.Z. and S.N.G.; Methodology, Z.Z., R.J.G, K.K., B.B., and S.N.G.; Software, Z.Z., H.L. N.G., and S.N.G.; Validation, Z.Z., H.L., and J.J.L.; Formal Analysis, Z.Z., J.J.L., H.L.; Investigation, Z.Z., H.L., and S.N.G.; Resources, Z.Z., K.K., B.B., and S.N.G.; Data Curation, Z.Z., H.L., and J.J.L.; Writing – Original Draft, Z.Z., and S.N.G.; Writing – Review & Editing, Z.Z., H.L., J.L., N.G., R.J.G., K.K., B.B., and S.N.G.; Visualization, Z.Z., H.L., J.J.L.; Supervision, S.N.G.; Project Administration, S.N.G.; Funding Acquisition, S.N.G.

Competing interests

The authors declare no competing interests.

Data and materials availability

The datasets generated and analyzed in the current study are available in the Dryad repository, [to finalize].

Supplementary Materials

Supplementary Data

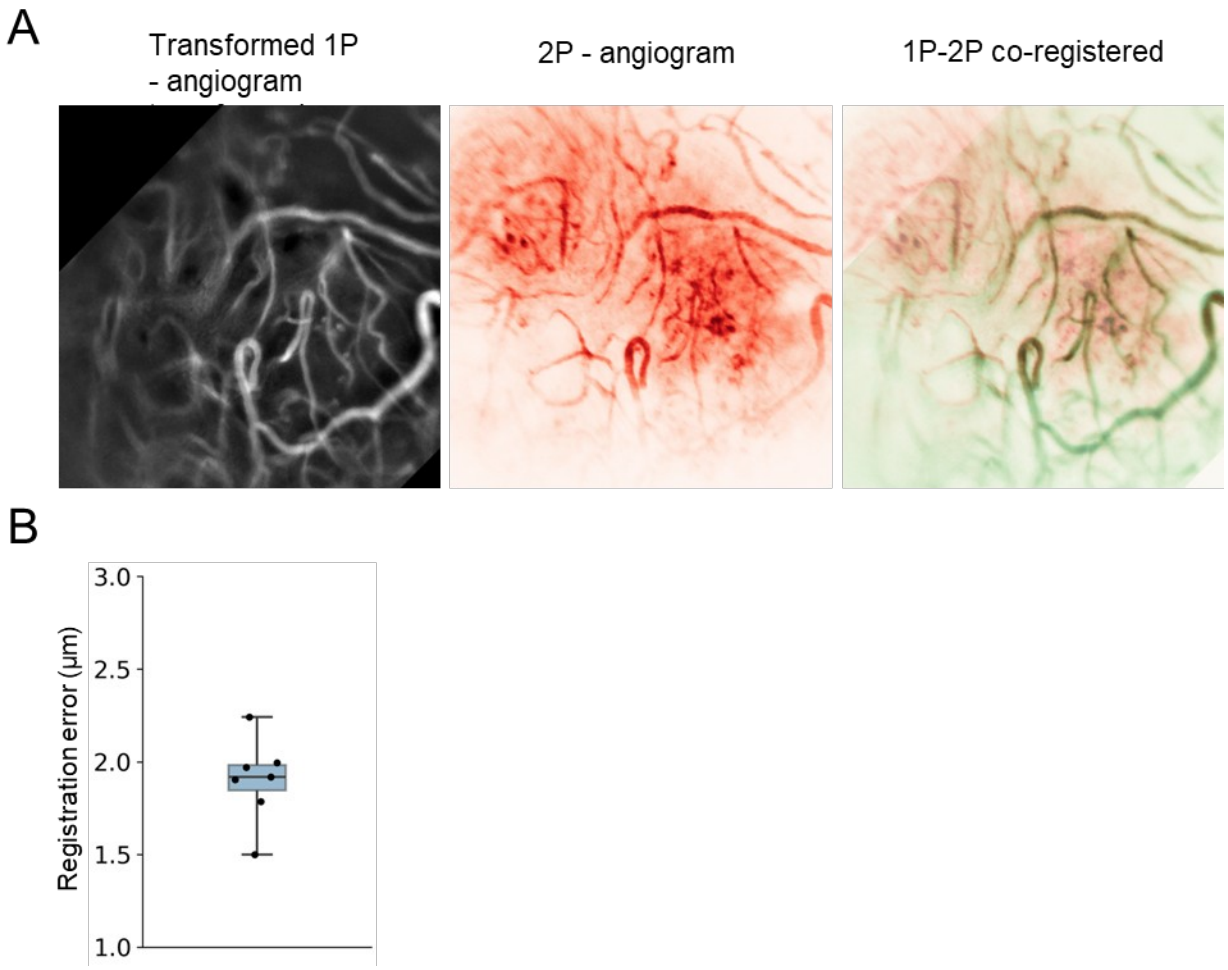

Suppl. Figure 1. Co-registration of 1P and 2P angiograms
(A) 1P neuronal and 2P plaque images were co-registered using angiogram fiducials via rigid transformation. (B) Root mean square error of the distances between transformed 1P and imaged 2P vessels. Box plot show the median (central line), the 25th and 75th percentiles (box edges), and whiskers extending to the minimum and maximum values.

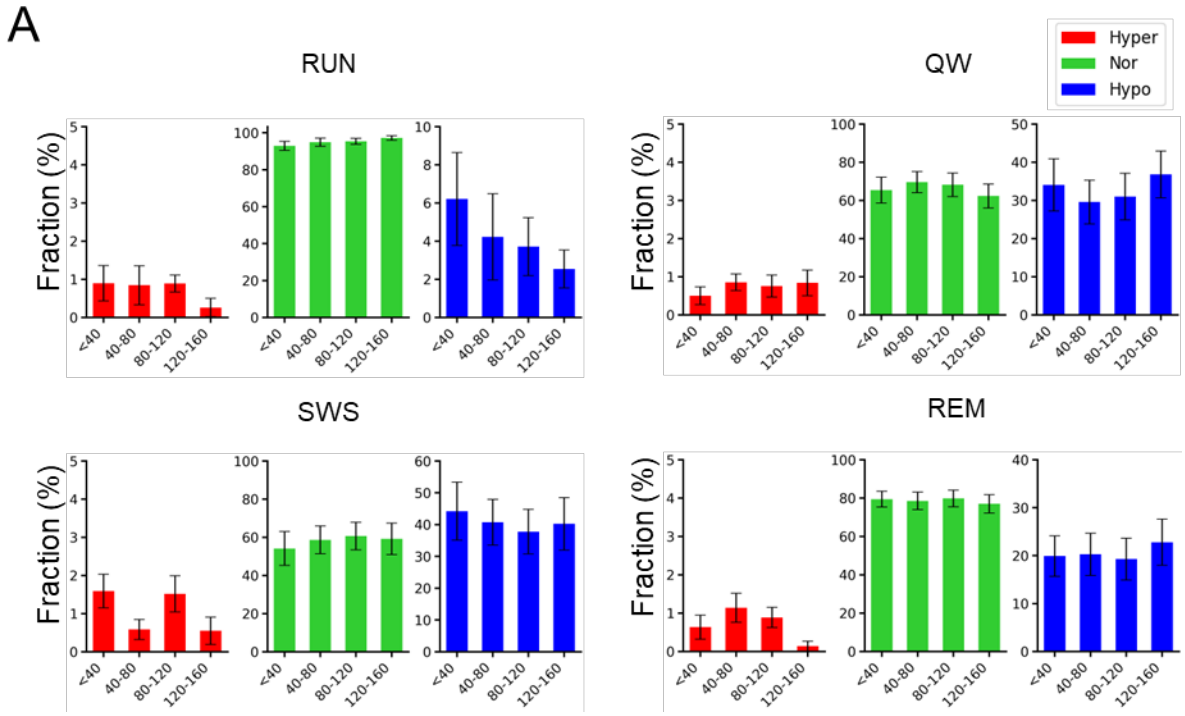

Suppl. Figure 2. Proportions of Hyperactive (red), Normal (green), and Hypoactive (blue) neurons as a function of distance from the nearest plaque, for each behavioral state. Here, hyperactive cells are defined for each state as those cells with the top 1% event rates. n=7 mice, 3762 cells. Error bars represent the mean ± standard error.

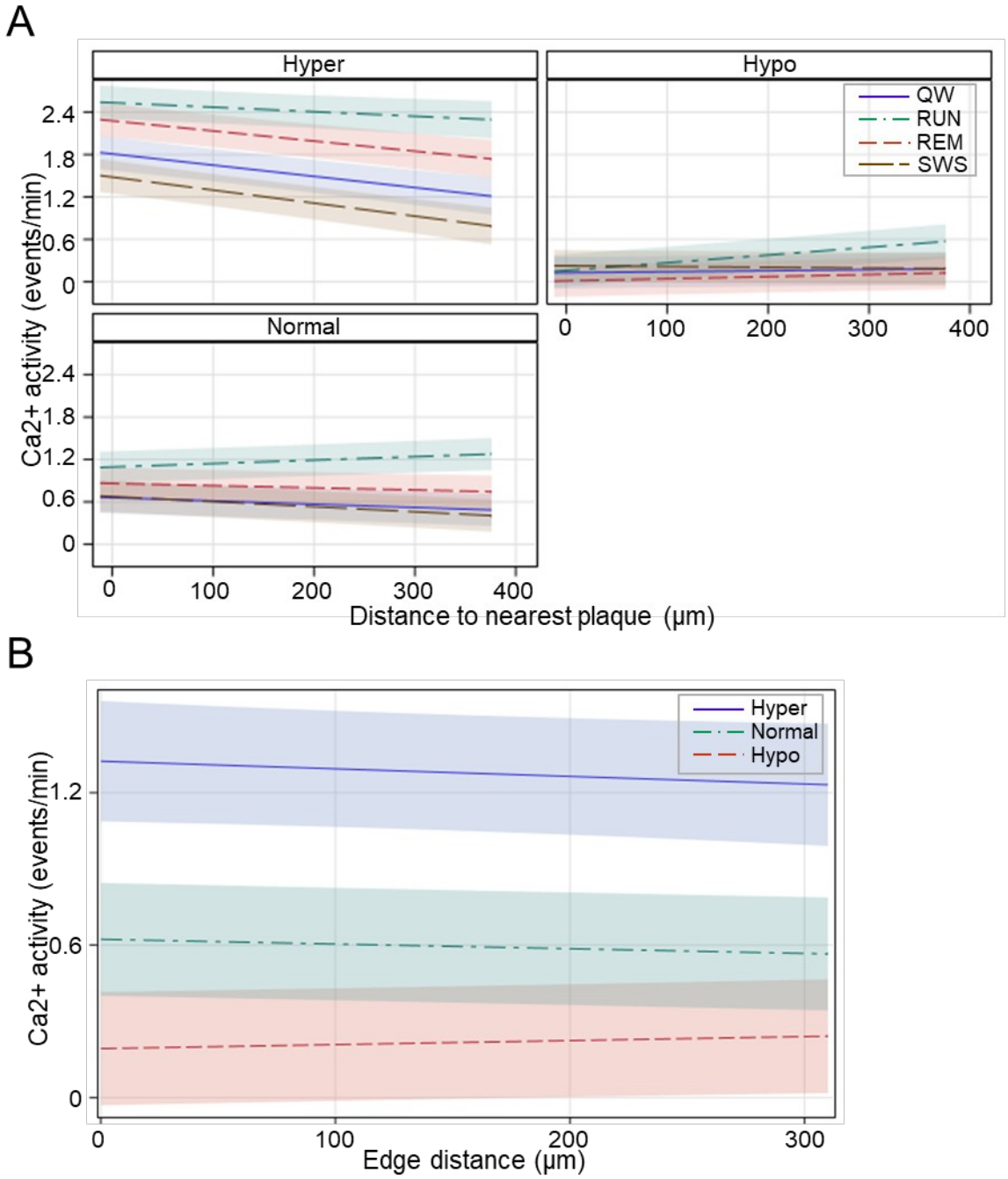

Suppl. Figure 3. Effect of cell activity type and behavioral state on calcium activity as a function of distance to nearest plaque and on edge distance (A) Calcium activity of Hyperactive, Hypoactive and Normal rate cells for each behavioral state differs as a function of distance from the nearest plaque (mixed effects model, $p<0.0001$). n=7 mice, 3762 cells. (B) Calcium activity as a function of distance from the Edge of the field of view for Hyperactive, Hypoactive and Normal rate cells (mixed effects model, $p=0.0065$). Data are represented as best fit with 95% confidence limits.

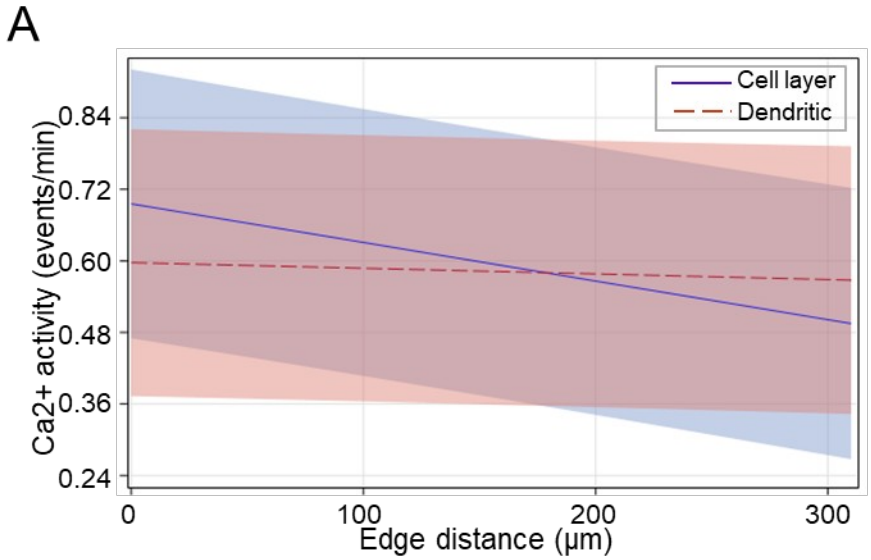

Suppl. Figure 4. Interaction between plaque axial position and edge distance Calcium activity as a function of distance from the Edge of the field of view stratified by nearest plaque axial position (mixed effects model, $p<0.0001$). Data are represented as best fit with 95% confidence limits.

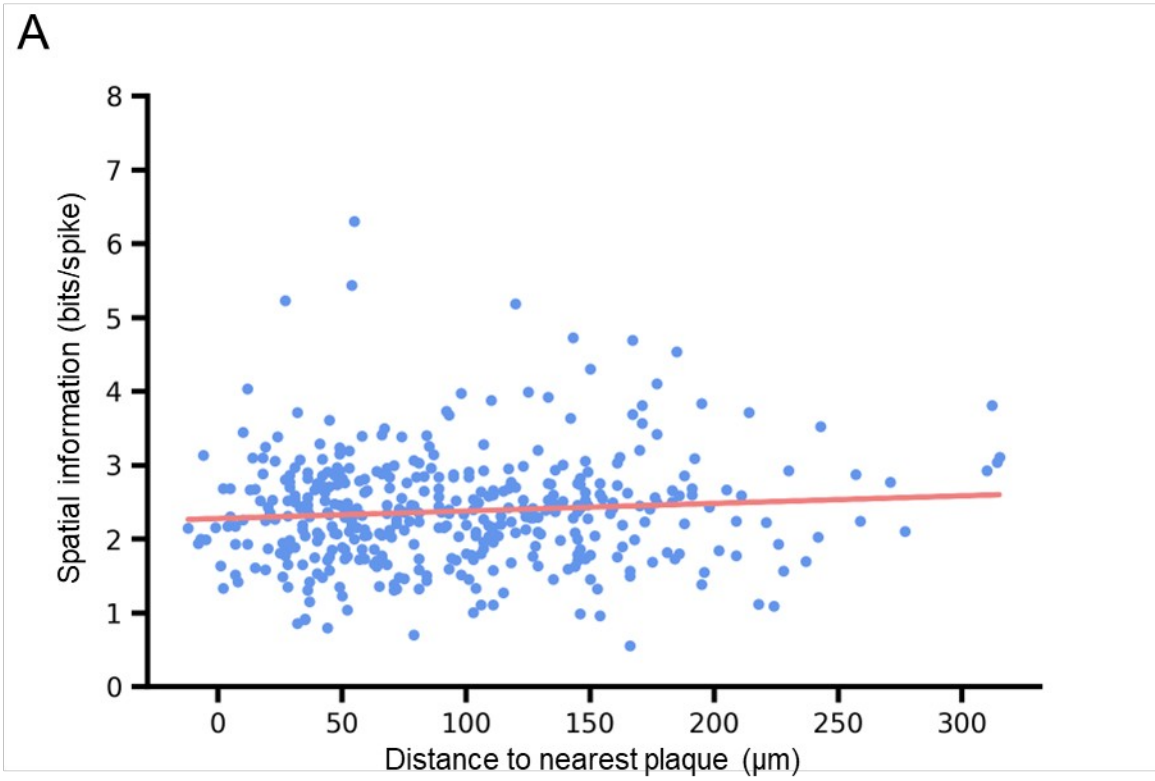

Suppl. Figure 5. Place cell spatial information does not depend on proximity to amyloid plaques. Red line, linear least squares regression fit (r = 0.086, p=0.08). Mixed effects model, n.s.

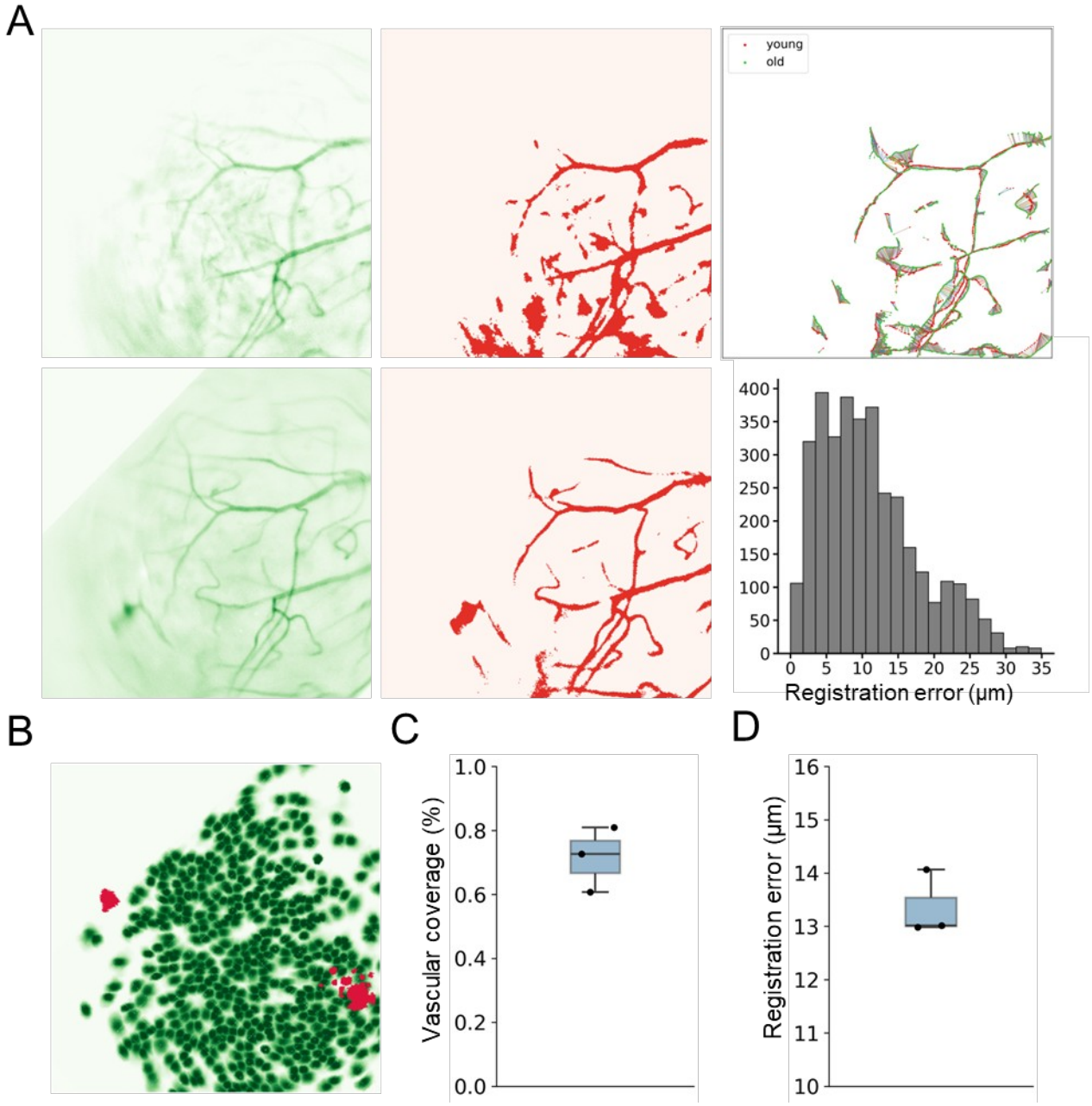

Suppl. Figure 6. Coregistration of young and old datasets (A) Mapping vessels at 2 time-points in order to coregister neuronal dynamic calcium activity before plaques form to future plaque locations. (Left) 1P angiogram of a representative mouse at 6.2 months (top) and 10.5 months (bottom). (Middle) Vessel identification of young (top) and old (bottom) datasets. (Right, top) Identified vessels of young and old datasets, superimposed using rigid body transformation. (Right, bottom) Registration error of these datasets. (B) Co-registered imaged somas at 6.2 months and plaques at 10.5 months. (C) Vascular coverage of the field of co-registered imaged cells and plaques. (D) The root mean square error of the distances between transformed young and old 1P vessels. Box plots show the median (central line), the 25th and 75th percentiles (box edges), and whiskers extending to the minimum and maximum values.

Figure captions

Figure 1. Mapping hippocampal dynamic calcium activity to amyloid plaques in a freely behaving AD mouse (A) Schematic of 1-photon (1P) miniscope hippocampal dynamic calcium imaging and local field potential (LFP) recording in freely behaving mice and subsequent 2-photon (2P) imaging of amyloid plaques. (B) Representative experiment. Upper panel: LFPs recorded in CA1 during exploratory behavior (RUN), quiet wakefulness (QW), slow wave sleep (SWS), and rapid eye movement sleep (REMs). Lower panel: Calcium traces from representative cells in each behavioral state. High, normal, and low activity are shown in red, green, and blue, respectively. (C) 1P-imaged GCaMP6f dynamic calcium activity (somas in white (left)), 2P-imaged Methoxy-X04 labeled amyloid plaques, red (middle), and 1P-calcium activity (somas in green) co-registered with 2P-amyloid plaques (red) (right). Cells in b are marked. (D) Proportions of Hypoactive (blue), Normal (green), and Hyperactive (red) neurons as a function of distance from the nearest plaque (n=7 mice), for each behavioral state. Note an absence of focal clustering of hyperactive cells near amyloid plaques. n=7 mice, 3762 cells. Error bars represent the mean ± standard error.

Figure 2. Dynamic calcium activity depends on proximity to amyloid plaques (A) Maps of hippocampal dynamic calcium activity co-registered with amyloid plaques (white) in each behavioral state of a representative experiment. The state-specific thresholds for hypoactivity and hyperactivity are labeled in each colorbar. Scale bar, 100 μm. (B) Calcium activity for each behavioral state differs as a function of distance from the nearest plaque for Hyperactive, Hypoactive and Normal rate cells (mixed effects model, $p<0.0001$). n=7 mice, 3762 cells. Data are represented as best fit with 95% confidence limits.

Figure 3. Effect of hippocampal axial position and plaque size on dynamic calcium activity (A) Representative examples of amyloid plaques (red) relative to GCaMPF-expressing cells in the pyramidal cell layer (green). (top) Axial view, differentiating 'cell layer' and 'dendritic' plaques. (bottom) Superior view. (B) Distribution of plaque diameters of cell layer and dendritic plaques (n=7 mice). The gray line indicates the threshold determined by k-means clustering. (C) Calcium rates fell faster with increasing distance from cell layer plaques than dendritic plaques, and this effect was greatest for big plaques (mixed effects model, $p=0.0039$). n=7 mice, 3762 cells. Fits are computed at edge distance 136.6 mm, SWS, for normal rate cells. Data are represented as best fit with 95% confidence limits.

Figure 4.Evaluating the spatial relationship of place cells and amyloid plaques (A) Location of calcium events (red) of a representative place cell as a mouse traverses a linear track. (B) Place cells sorted by their place field locations for inbound (LR) and outbound (RL) directions. Color bar indicates probability. The place field of each cell is shown in yellow.(C) Proportion of imaged place cells to total CA1 cells in wild-type (n=4) and APP/PS1 mice (n=7; mean ± S.E.M.). (D) Representative image showing hippocampal place cells (cyan) and non-place cells (gray) co-registered with amyloid plaques (white). (E) (Top) Distribution of inter-cell distances for WT (blue) and APP/PS1 (red) place cells, highlighting an increased proportion of small distances in APP/PS1 mice. Vertical line, 75 μm. (Bottom) The eCDF of inter-cell distances differs for WT and APP/PS1 mice (K-S test, $p<10^{-14}$) (Inset: full eCDF). (F) In APP/PS1 mice, place cell probability increased with proximity to the nearest amyloid plaque (mixed effects model, $p<0.0001$). This effect increased with greater distance from the edge of the field of view, as shown for three edge distances defined in the inset (mixed effects model,

$p<0.0001$). Place cell probability was higher near dendritic layer plaques than cell layer plaques. *, $p<0.05$ Control n=4 mice, 559 place cells, 2468 total cells; APP/PS1 n=7 mice, 410 place cells, 3762 total cells. Data are represented as best fit with 95% confidence limits.

Figure 5. Mapping place cell locations before plaques form to future plaque locations (A) Representative experiment. Co-registration of 1-P angiogram fiducial before plaques form (Left) and 2-P angiogram fiducial after plaques form (middle) to co-register dynamic calcium activity before plaques form to imaged plaques. (B) Distance to nearest future plaques was similar for place cells and nonplace cells (n.s.). Box plots show the median (central line), the 25th and 75th percentiles (box edges), and whiskers extending to the minimum and maximum values. (C) Greater dynamic calcium activity in SWS before plaques formed was associated with smaller distance to the nearest future amyloid plaque (mixed effects model, $p=0.038$). n=3 mice, 1080 cells. Data are represented as best fit with 95% confidence limits.

Figure 1

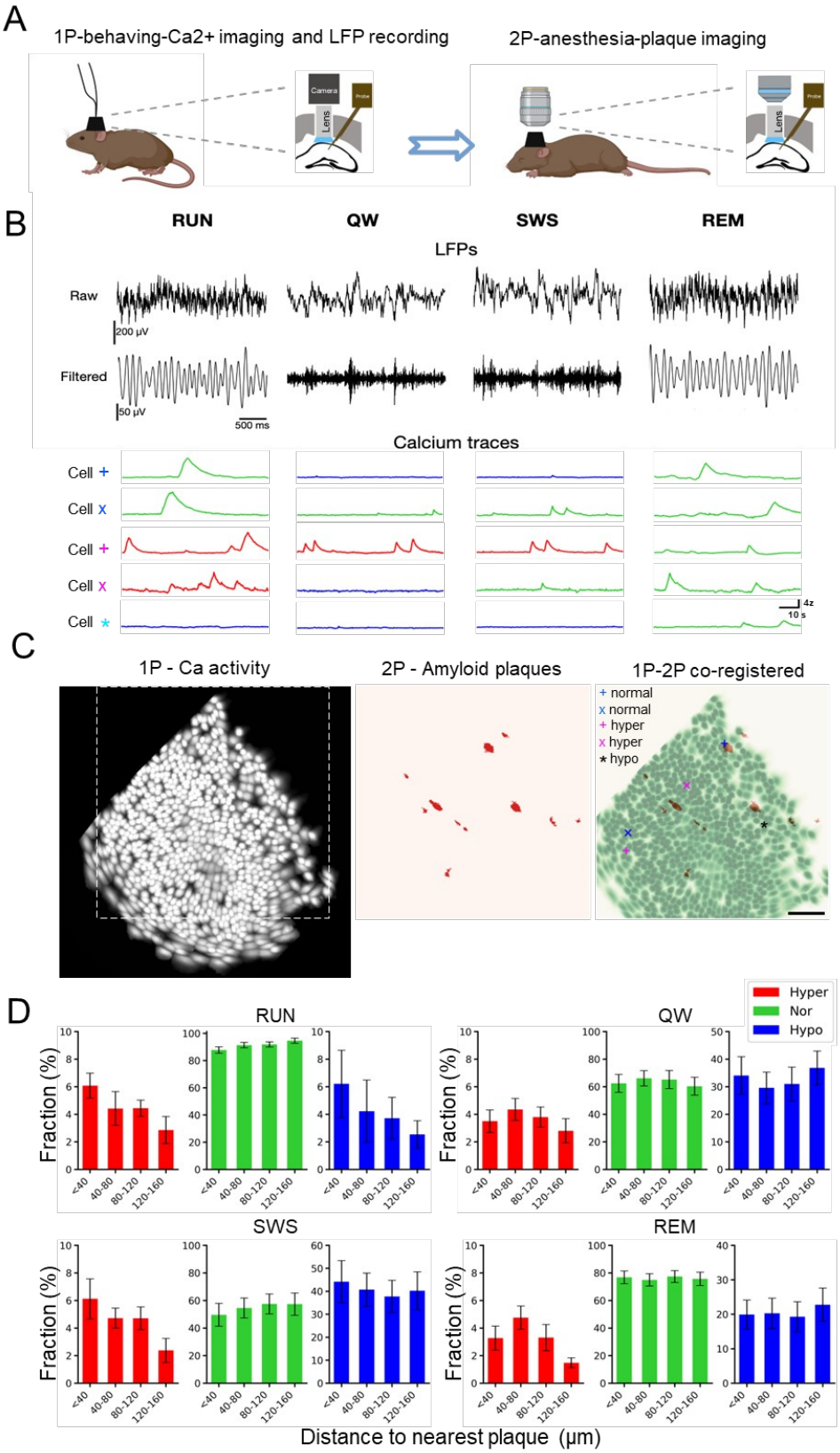
A
1P-behaving-Ca2+ imaging and LFP recording
2P-anesthesia-plaque imaging
Camera
Lens
Probe
B
RUN
QW
SWS
REM
LFPs
Raw
200 µV
Filtered
50 µV
500 ms
Calcium traces
Cell +
Cell x
Cell +
Cell x
Cell *
10 s
C
1P - Ca activity
2P - Amyloid plaques
1P-2P co-registered
+ normal
x normal
+ hyper
x hyper
* hypo
D
Hyper
Nor
Hypo
RUN
QW
SWS
REM
Fraction (%)
<40
40-80
80-120
120-160
Distance to nearest plaque (µm)

Figure 2

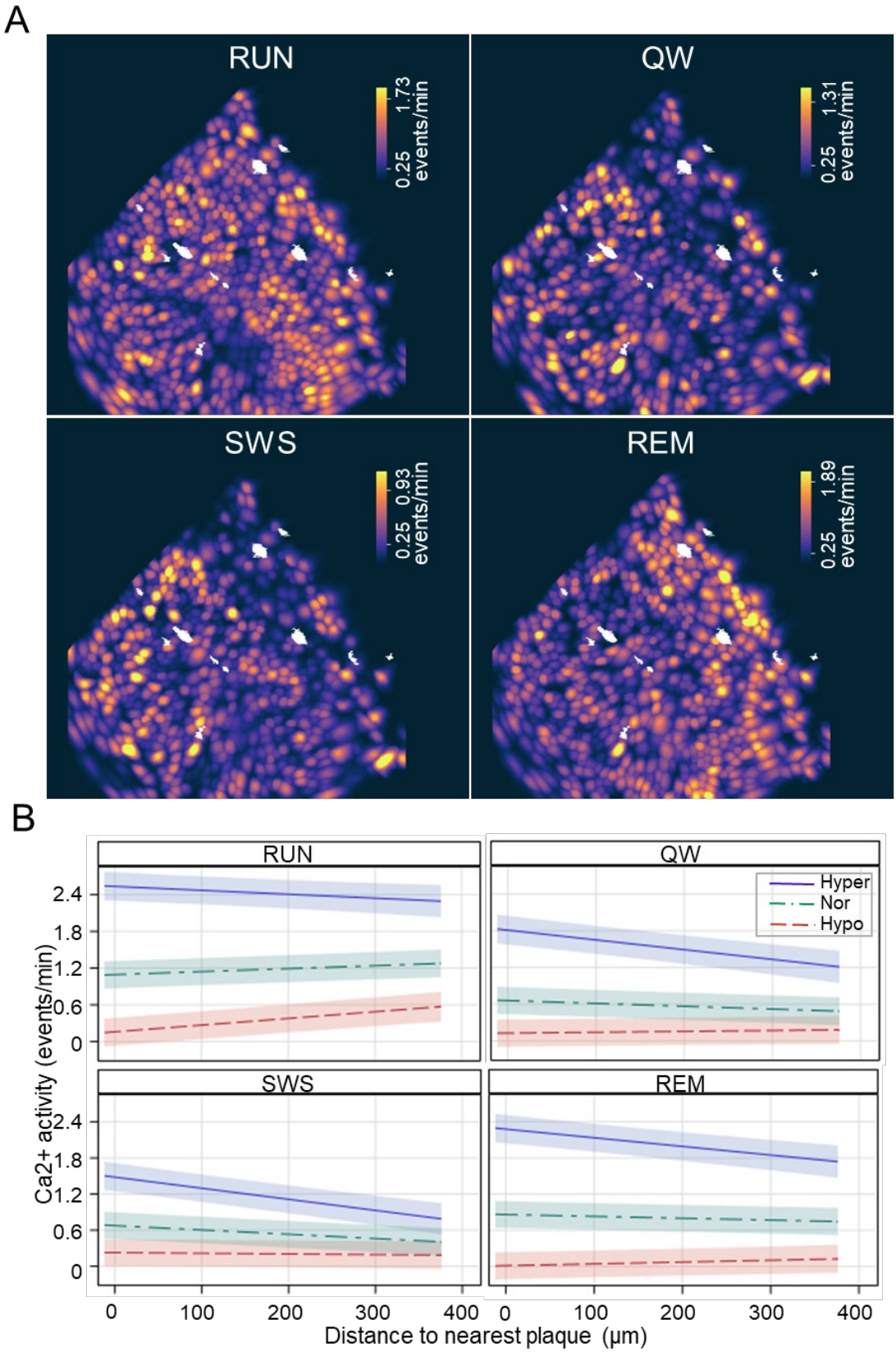
A
RUN
0.25
1.73
events/min
QW
0.25
1.31
events/min
SWS
0.25
0.93
events/min
REM
0.25
1.89
events/min
B
RUN
QW
SWS
REM
Hyper
Nor
Hypo
Ca2+ activity (events/min)
2.4
1.8
1.2
0.6
0
0
100
200
300
400
Distance to nearest plaque (μm)

Figure 3

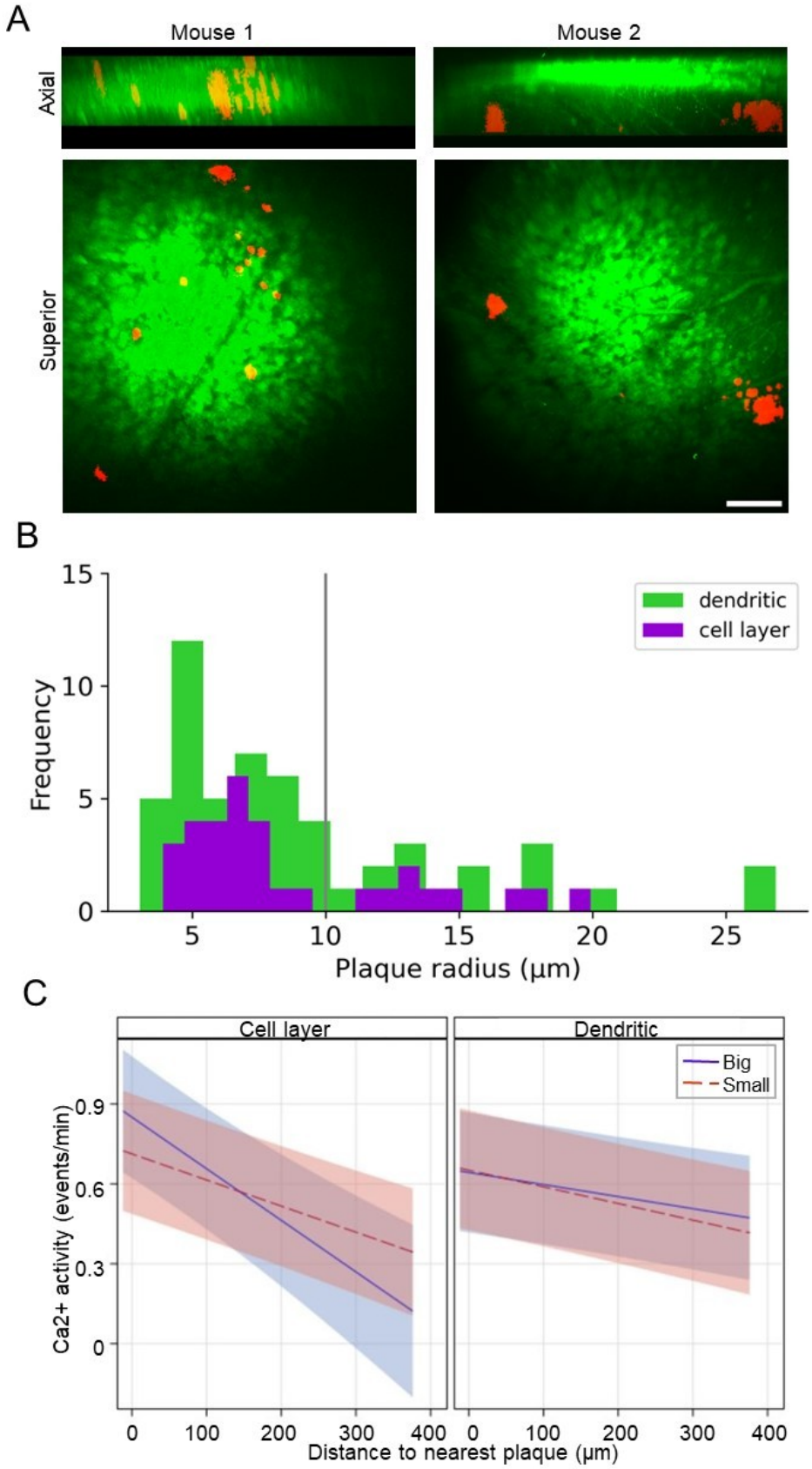
A
Mouse 1
Mouse 2
Axial
Superior
B
dendritic
cell layer
Frequency
Plaque radius (µm)
C
Cell layer
Dendritic
Big
Small
Ca2+ activity (events/min)
Distance to nearest plaque (µm)

Figure 4

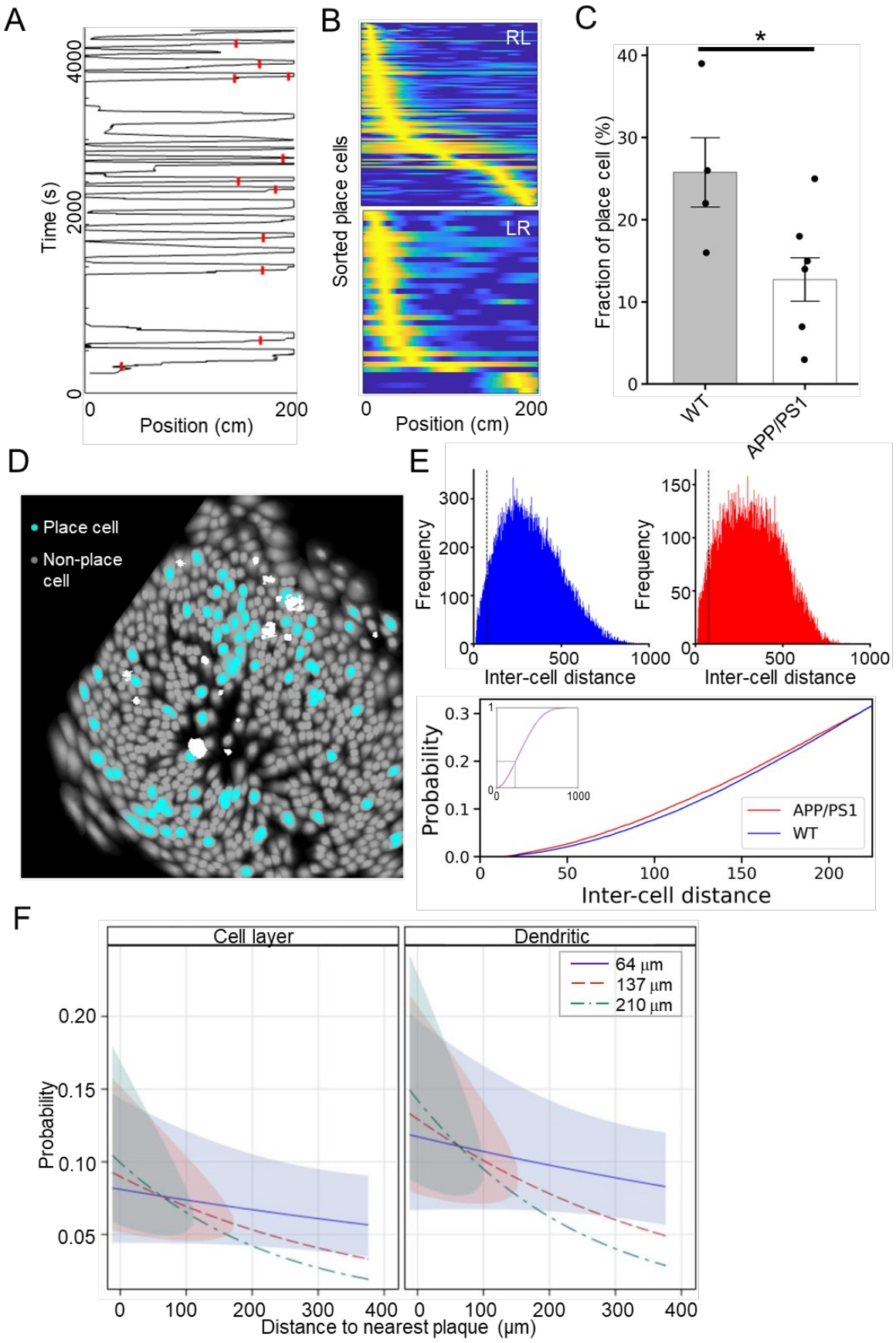
A
Time (s)
4000
2000
0
0
200
Position (cm)
B
RL
LR
Sorted place cells
0
200
Position (cm)
C
*
Fraction of place cell (%)
40
30
20
10
0
WT
APP/PS1
D
Place cell
Non-place cell
E
Frequency
300
200
100
0
500
1000
Inter-cell distance
Frequency
150
100
50
Inter-cell distance
Probability
0.3
0.2
0.1
0.0
0
50
100
150
200
Inter-cell distance
APP/PS1
WT
F
Cell layer
Dendritic
64 µm
137 µm
210 µm
Probability
0.20
0.15
0.10
0.05
0
100
200
300
400
Distance to nearest plaque (µm)

Figure 5

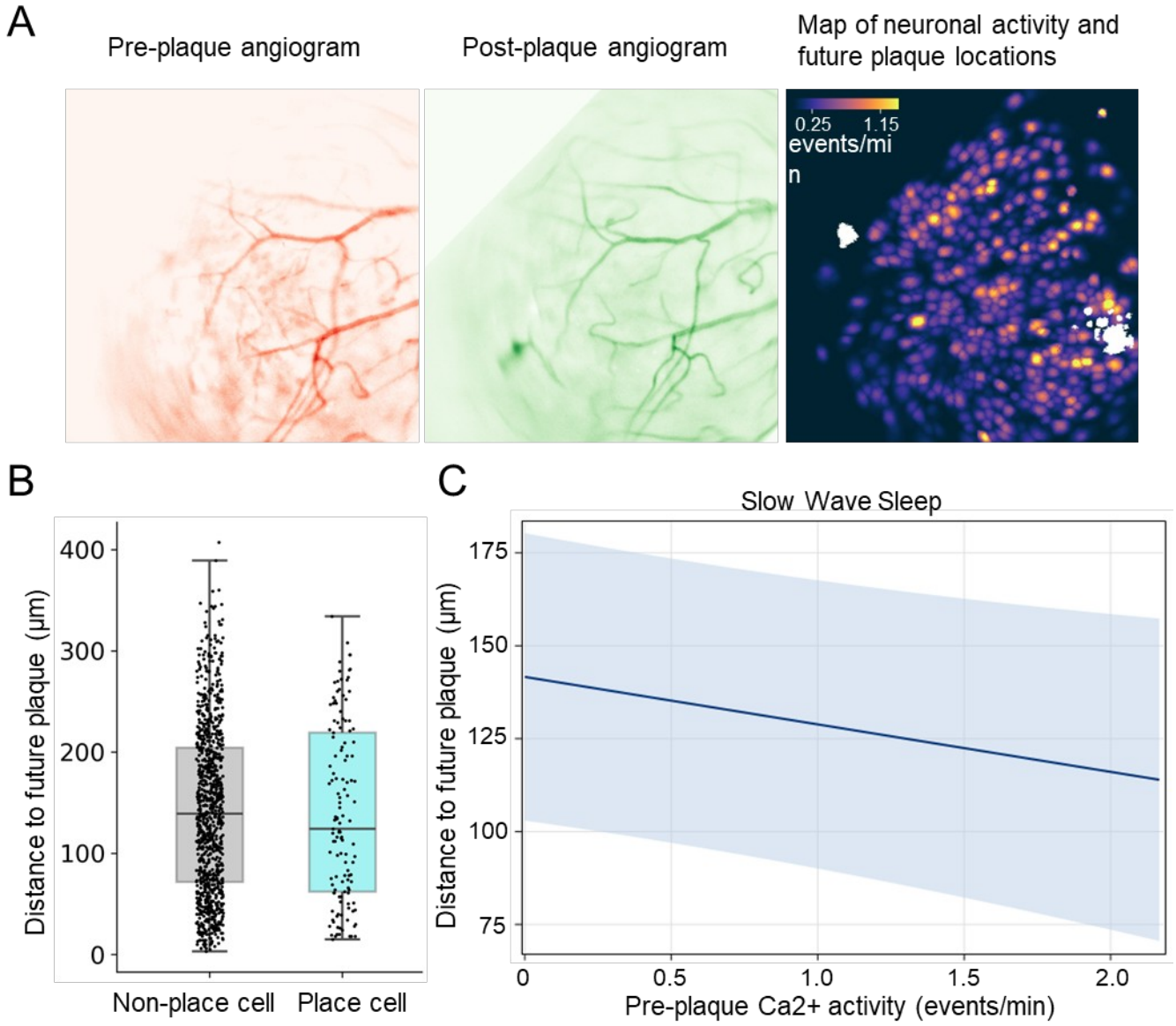
A
Pre-plaque angiogram
Post-plaque angiogram
Map of neuronal activity and future plaque locations
0.25
1.15
events/min
B
Distance to future plaque (µm)
400
300
200
100
0
Non-place cell
Place cell
C
Slow Wave Sleep
Distance to future plaque (µm)
175
150
125
100
75
0
0.5
1.0
1.5
2.0
Pre-plaque Ca2+ activity (events/min)